ACS APPLIED MATERIALS & INTERFACES

Research Article

www.acsami.org

Fabrication of Free-Standing $ZnMn_2O_4$ Mesoscale Tubular Arrays for Lithium-Ion Anodes with Highly Reversible Lithium Storage Properties

Jong Guk Kim,[†,‡] Sang Ho Lee,[†,‡] Youngmin Kim,[†,‡] and Won Bae Kim*[,†,‡]

[†]School of Materials Science and Engineering, Gwangju Institute of Science and Technology (GIST), 261 Cheomdan-gwagiro, Buk-gu, Gwangju 500-712, South Korea

[‡]Research Institute for Solar and Sustainable Energies (RISE), Gwangju Institute of Science and Technology (GIST), 261 Cheomdan-gwagiro, Buk-gu, Gwangju 500-712, South Korea

Supporting Information

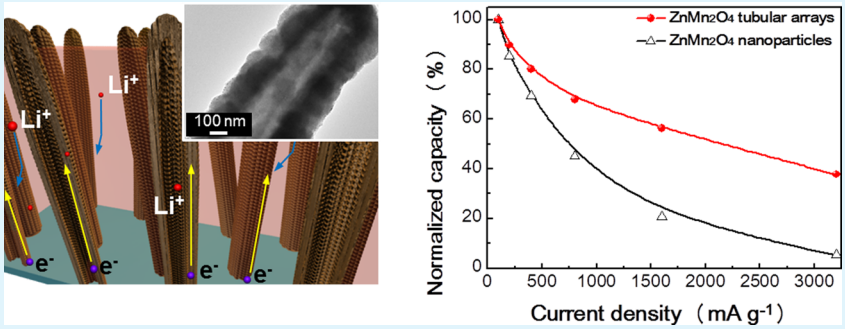

ABSTRACT: In this paper, $ZnMn_2O_4$ mesoscale tubular arrays on current collectors were successfully synthesized using a reactive template route combined with a postcalcination process through the shape-preserving conversion of ZnO nanorod arrays in aqueous solutions at room temperature. On the basis of the experimental analyses, including X-ray diffraction, Raman spectroscopy, scanning electron microscopy, and transmission electron microscopy, a plausible formation mechanism of $ZnMn_2O_4$ tubular arrays was proposed in which solid ZnO nanorods are gradually transformed to $ZnMn_2O_4$ tubules via a simple cation exchange process between Zn^{2+} and Mn^{2+}, followed by a postannealing process. Moreover, the lithium storage properties of the as-prepared $ZnMn_2O_4$ tubular structures were investigated by applying the structures as an active electrode material without auxiliary additives. The $ZnMn_2O_4$ array electrodes showed an excellent discharge capacity of ca. 1198.3 mAh g^{-1} on the first cycle and exhibited outstanding cycling durability, rate capability, and Coulombic efficiency. These results indicate that the free-standing tubular array architectures of $ZnMn_2O_4$ prepared directly on the current collector can be powerful candidates for a highly reversible lithium storage electrode platform.

KEYWORDS: *direct growth, one-dimensional, free-standing $ZnMn_2O_4$ tubular arrays, aqueous cation exchange, Li-ion batteries*

INTRODUCTION

The ever-growing demands for the high capacity and cycling durability of lithium-ion batteries (LIBs) have led to tremendous research efforts for the development of advanced electrode materials.[1] Specifically, various nanostructured 3d transition-metal oxides, such as CuO,[2,3] Fe_3O_4,[4,5] Co_3O_4,[6] NiO,[7] ZnO,[8] and Mn_3O_4,[9−11] have been extensively investigated as potential anode materials due to their high specific capacity, safety, and abundance.[1] Among them, manganese oxides have received increasing attention as a promising substitute for current commercial graphite anodes due to their low operating voltage, low toxicity, low cost, and abundance.[9−11] However, the practical application of manganese oxides to LIB electrodes is hampered by its poor electronic conductivity and large volume variation during repeated charge/discharge processes, which could lead to cracking with subsequent electrical insulation and rapid capacity decrease.[4,12,13] Recently, spinel structured ternary manganese oxides, such as $CoMn_2O_4$,[14] $NiMn_2O_4$,[15] and $ZnMn_2O_4$,[16−25] have attracted great interest for improving the capacity retention of manganese-based electrodes. $ZnMn_2O_4$ has been proposed as a practical alternative anode material for LIBs because of its low oxidation potentials (i.e., delithiation potential) of zinc and manganese at 1.2 and 1.5 V (versus Li/Li^+), respectively. These low oxidation potentials could eventually increase the battery output voltage compared to Co_3O_4, NiO, or CuO, thus allowing the delivery of a higher energy density.[16−25] Furthermore, zinc and manganese are abundant, environmentally friendly, and relatively inexpensive compared to nickel and cobalt.

Received: August 22, 2013
Accepted: October 14, 2013
Published: October 14, 2013

The inorganic tubular, or hollow, structured materials have gained significant interest due to their unique physicochemical properties and possible widespread applications in various areas.[26−28] In particular, tubular structured materials have been intensively studied as alternative LIB electrodes, with long-term cyclability and a highly reversible electrode reaction as a result of their ability to ameliorate the induced mechanical stress more effectively during repetitive cycling.[29,30] To synthesize the hollow structured materials, various template-based methods have been used, such as nonreactive or reactive template routes.[26,31] When a nonreactive hard template is used to prepare the hollow materials, an extra step involving template removal is inevitably necessary. However, this process is not required in the reactive template method because the template itself acts as both a reactant and a template.[32] Therefore, the reactive template methodology could control both the shape and the composition of the as-fabricated hollow materials. Consequently, the reactive template route is a more straightforward and effective way to fabricate the tubular structures with desirable compositions.[33] Unfortunately, however, only a few materials have been found to be suitable for tubular structure synthesis through the cation exchange routes, and it also remains a challenge to develop mesoscale tubules made of mixed metal oxides for highly stable LIB electrodes.[34−38]

Herein, we report a facile approach for the synthesis of mesoscale tubular arrays of $ZnMn_2O_4$ by employing the reactive template of ZnO nanorod arrays via the cation exchange method in aqueous solutions, combined with a postannealing process. To the best of our knowledge, this is the first time that mesoscale tubular arrays of spinel $ZnMn_2O_4$ structures have been applied to the LIB electrodes with highly stable charge/discharge properties. The synthesized $ZnMn_2O_4$ tubular array electrode shows an excellent initial discharge capacity (1198.3 mAh g^{-1}), long-term cycling stability, and high Coulombic efficiency. This hollow $ZnMn_2O_4$ array platform could fulfill the important requirements for LIB electrodes, such as mechanical stability, uniform coverage of the active materials, and numerous active sites for enhanced electrolyte permeability. Furthermore, the energy density of the electrodes could be increased because no auxiliary material is required in the system proposed herein, compared with the conventional electrodes that require powder mixing and slurry casting processes. From their unique architecture and high electrochemical performance, these $ZnMn_2O_4$ mesoscale tubular array electrodes could be considered promising electrodes for next-generation energy storage platforms.

EXPERIMENTAL DETAILS

Synthesis of $ZnMn_2O_4$ Tubular Arrays. The reactive templates of ZnO nanorod arrays were prepared on titanium (Ti) substrates (thickness = 0.127 mm, 99.7%, Aldrich) according to the previous literature.[29] For the fabrication of $ZnMn_2O_4$ mesoscale tubular arrays, the ZnO nanorod templates were immersed in a solution containing 50 mL of distilled water (18.2 MΩ cm) mixed with 0.98 g of $(CH_3COO)_2Mn{\cdot}4H_2O$ (≥99%, Aldrich). The reaction vessel was sealed and kept at room temperature for 72 h. After the reaction, the substrate was thoroughly washed with distilled water and ethanol to remove residual salts, and subsequently dried at 70 °C. The substrate was finally heat-treated in an Ar atmosphere at 500 °C for 4 h, to enhance the crystallinity of as-prepared $ZnMn_2O_4$ and further remove the residual chemicals.[35]

For comparison, $ZnMn_2O_4$ nanoparticles were also synthesized via a hydrothermal route. In a typical synthesis, 0.22 g of $(CH_3COO)_2Zn{\cdot}2H_2O$ (≥99%, Aldrich) and 0.49 g of $(CH_3COO)_2Mn{\cdot}4H_2O$ (≥99%, Aldrich) were dissolved in 50 mL of ethylene glycol. This solution was magnetically stirred for 20 min under atmospheric conditions and was hydrothermally heated to 160 °C and maintained at this temperature for 12 h, followed by cooling to room temperature. The resulting material was rinsed thoroughly with distilled water and ethanol and then dried in a convection oven at 70 °C.

Physicochemical Characterization and Electrochemical Measurements. Measurements using scanning electron microscopy (SEM) were conducted with a JEOL JSM-7500F. The X-ray diffraction (XRD) patterns were recorded with a Rigaku Rotalflex RU-200B diffractometer using a Cu−Kα (λ = 1.5418 Å) source with a Ni filter at 40 kV, 40 mA, and a scan rate of 0.02° s^{-1}. Raman spectra (Renishaw, Invia) were obtained using 514 nm Ar^+ laser excitation. The spectra were recorded between 1000 and 100 cm^{-1}, and the laser power used for this characterization was 8.5 mW. Transmission electron microscopy (TEM) and high-resolution TEM (HRTEM) observations were carried out (Tecnai G2 F30 S-Twin) at 300 kV. These observations were coupled with energy-dispersive X-ray spectrometry (EDX). X-ray photoelectron spectroscopy (XPS, ESCALAB 250) analysis was conducted using a monochromic Al−Kα X-ray source (E = 1486.6 eV). Data processing of the XPS measurements was performed with the XPSPEAK software program.

The $ZnMn_2O_4$ arrays on the Ti substrates were directly employed as a working electrode without addition of any conductive agents or cohesive binders. The mass of the as-prepared $ZnMn_2O_4$ arrays was measured using a microbalance (Sartorius, M3P) by weighing the sample before and after the synthesis process. The measured mass of $ZnMn_2O_4$ mesoscale tubular arrays on the substrate was about ca. 0.49 mg cm^{-2}. Prior to the battery cycling tests, the electrode was dried in a vacuum oven overnight at 120 °C. The electrolyte consisted of 1 M $LiPF_6$ in a 1:1 v/v mixture of ethylene carbonate and diethyl carbonate (Cheil Industries). Pure lithium foil was used as a counter electrode, and Cellgard 2400 was used as a separator film. The cell (CR2032 coin type) was assembled in an argon-filled glovebox in which the moisture and oxygen concentrations were maintained below 1 ppm. For comparison, a reference electrode made of $ZnMn_2O_4$ nanoparticles was also prepared, which was composed of 60 wt % $ZnMn_2O_4$, 20 wt % carboxylmethyl cellulose binder, and 20 wt % carbon black. The cells were aged for 24 h before the electrochemical measurements, and the cyclic voltammograms (CVs) were performed at a scan rate of 0.05 mV s^{-1} from 3.0 to 0.01 V with an AMETEK Solartron Analytical 1400. The fabricated cells were also galvanostatically cycled at a rate of 100 mA g^{-1} between 0.01 and 3.0 V on a WBCS 3000 battery tester (WonA Tech).

RESULTS AND DISCUSSION

Figure 1a shows a representative SEM image of the ZnO nanorod arrays grown on Ti substrates, which were used as the reactive template for the synthesis of the $ZnMn_2O_4$ mesoscale tubular arrays in this work. The image shows that the ZnO nanorods stand almost vertically on the Ti substrate and uniformly cover the substrate surface. The inset of Figure 1a reveals the needle-like configuration of individual ZnO nanorods with sharp tips of 50 nm or smaller. The $ZnMn_2O_4$ tubular arrays were synthesized through the cation exchange route at room temperature, as shown in Figure 1b. Note that the $ZnMn_2O_4$ tubular arrays maintain their original 1D ZnO template after the reaction. However, in contrast to the smooth surface of the ZnO nanorods, the converted $ZnMn_2O_4$ structures appear to have rather rough surfaces. Most of $ZnMn_2O_4$ arrays exhibited closed tips; however, the hollow interior could be identified from broken parts of the array structure, as demonstrated in the inset of Figure 1b. The 1D tubular structures of the $ZnMn_2O_4$ arrays show their wall thickness of approximately 150 nm. The $ZnMn_2O_4$ tubular arrays with closed tips also stand almost vertically on the substrate. Conformal contact between the $ZnMn_2O_4$ arrays and the Ti substrates can thereby be achieved

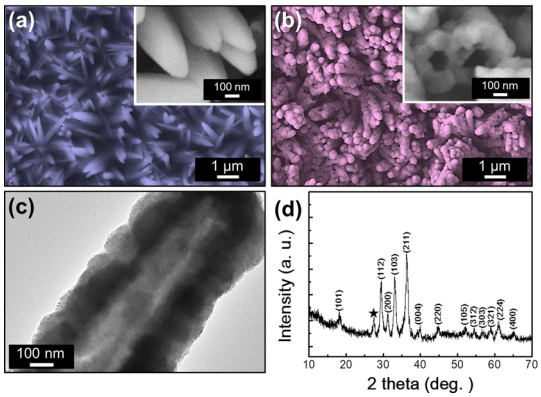

Figure 1. Typical SEM images of ZnO nanorod arrays (a) and $ZnMn_2O_4$ mesoscale tubular arrays (b). The inset images show the enlarged tips of ZnO and $ZnMn_2O_4$ arrays. In particular, the inset in panel (b) shows the enlarged tips of broken $ZnMn_2O_4$, revealing the tubular structure. (c) TEM image and (d) XRD patterns of $ZnMn_2O_4$ tubular arrays.

after the cation exchange reaction. This characteristic is significant for efficient charge transport when the array structures are employed in LIB electrodes.[29,30] Furthermore, the tubular array architectures of the as-prepared individual $ZnMn_2O_4$ tubules can be observed clearly in the TEM image in Figure 1c. Even in the TEM, the overall configuration of the 1D $ZnMn_2O_4$ tubular arrays remains intact after the reactions (see Figure S1 in the Supporting Information). The $ZnMn_2O_4$ mesoscale tubules exhibit a wall thickness of approximately 150 nm and distinct hollow structures, which are in agreement with the SEM observations. The crystal phase identification of the prepared architectures was performed using XRD measurements. The diffraction peaks were unambiguously indexed to the $ZnMn_2O_4$ spinel phase (a = 5.720 Å, c = 9.245 Å, JCPDS 24-1133) in Figure 1d, revealing a complete conversion of the ZnO template to $ZnMn_2O_4$ tubular arrays on the Ti substrate.

To investigate the evolution of the $ZnMn_2O_4$ phase from the ZnO template, the intermediate products at different reaction times were observed through XRD measurements. Figure 2a shows the XRD patterns of the products synthesized at different reaction periods from the initial ZnO phase to the formation stage of the $ZnMn_2O_4$. The diffraction patterns of reactive ZnO templates are well-indexed to the wurtzite phase (a = 3.250 Å, c = 5.207 Å, JCPDS 36-1451). The intensity of the (002) peak in the diffraction patterns of ZnO templates is much higher than that of the other peaks, indicating a c-axis orientation of the ZnO nanorods on the substrate.[29] After 24 h of reaction time, the peak intensity of ZnO was largely decreased. When the reaction time was increased to 48 h, peaks originating from the $ZnMn_2O_4$ phase were observed, while the ZnO peaks disappeared. This result indicates that Zn^{2+} is substituted by Mn^{2+} through the cation exchange reaction process, which is in line with TEM images in Figure S2 (Supporting Information). After 72 h of reaction time, the XRD patterns indicate that the $ZnMn_2O_4$ in a spinel structure (a = 5.744 Å, c = 9.225 Å) was produced, as confirmed by the standard values (a = 5.720 Å, c = 9.245 Å, JCPDS 24-1133). The diffraction peaks are generally sharpened as the reaction progresses, and the c/a value of the as-synthesized $ZnMn_2O_4$ is 1.61, which is also consistent with the standard values of $ZnMn_2O_4$ materials. The extra peak marked with a star can be attributed to the partially oxidized TiO_2 phase (a = 4.584 Å, c = 2.953 Å, JCPDS 89-4920) from the Ti substrate. Aside from this oxidation peak of Ti, there were no notable peak shifts or intensity variations induced by secondary phases or impurities, which suggests that all of the ZnO nanorods were transformed completely into the crystalline $ZnMn_2O_4$ tubular arrays. Therefore, the spinel phase of $ZnMn_2O_4$ has been successfully prepared in this work.

Raman scattering can prove the vibrational modes of both crystalline and amorphous materials; therefore, it could provide complementary structural information to the XRD analysis.[39−43] Figure 2b shows the Raman spectra of ZnO nanorods and $ZnMn_2O_4$ mesoscale tubules measured at room temperature in the wavenumber range from 1000 to 100 cm^{-1}. The Raman spectra of ZnO nanorods show four strong peaks at 99.0, 329.4, 437.4, and 574.5 cm^{-1} for the wurtzite phase of ZnO with a highly crystalline nature.[39] In other words, the dominant peaks at 99.0 and 437.4 cm^{-1} are attributed to the low- and high-E_2 modes, respectively, and the peak at 329.4 cm^{-1} is assigned to the $E_{2H}-E_{2L}$ (multiphonon) mode. Additionally, a peak at 574.5 cm^{-1} originating from the E_{1L} mode was observed.[40] After the full transformation from ZnO nanorods into $ZnMn_2O_4$ tubules, the peaks corresponding to ZnO completely disappeared, and three new peaks appeared at 322.2, 380.0, and 676.8 cm^{-1} from the spinel $ZnMn_2O_4$ phase, as shown in Figure 2b. In the spinel oxides, the modes above 600 cm^{-1} are attributed to the motion of oxygen in the tetrahedral AO_4 group; therefore, the peak at 676. 8 cm^{-1} is considered to indicate A_{1g} symmetry. The other low-frequency modes are characteristic of the octahedral BO_6 site. These peak positions are in good agreement with those previously reported for $ZnMn_2O_4$ materials[41−44] and support again the assumption of the complete transformation of ZnO nanorods into $ZnMn_2O_4$ tubules after the cation exchange reaction.

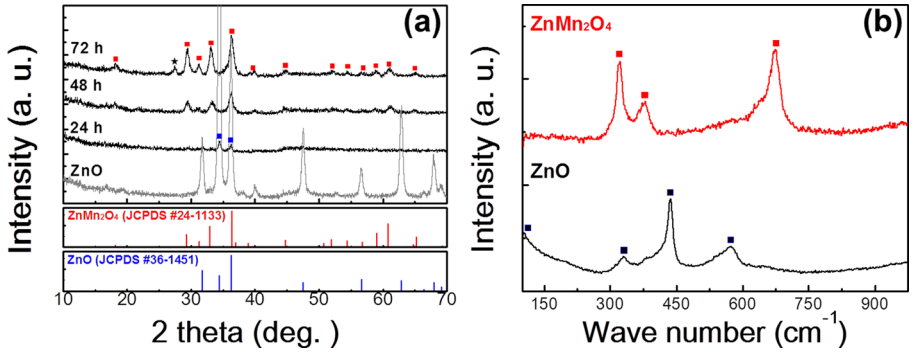

Figure 2. (a) XRD patterns of the products obtained at different reaction times. (b) Raman spectra of the ZnO and $ZnMn_2O_4$ materials.

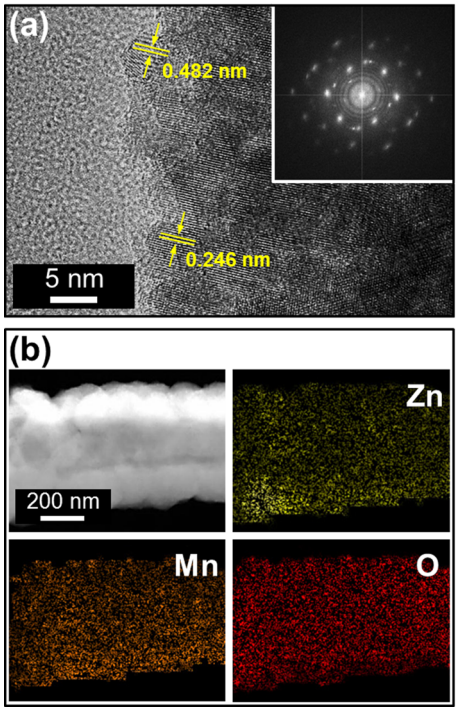

Figure 3. (a) HRTEM images of the $ZnMn_2O_4$ mesoscale tubules. The inset in panel (a) shows a corresponding SAED pattern. (b) Dark-field TEM image with corresponding elemental mappings of Zn, Mn, and O for the $ZnMn_2O_4$ mesoscale tubules.

The detailed structural properties of the $ZnMn_2O_4$ mesoscale tubules were further characterized by HRTEM. As shown in Figure 3a, lattice fringes with *d* spacings of 0.246 and 0.482 nm were observed, which is in accordance with the (211) and (101) interplanar spacings of the spinel $ZnMn_2O_4$, respectively, indicating the polycrystalline nature of the $ZnMn_2O_4$ tubules. The polycrystalline nature of the $ZnMn_2O_4$ mesoscale tubules is further confirmed by the presence of multiple diffraction rings in the selected area electron diffraction (SAED) patterns. The elemental distribution in the $ZnMn_2O_4$ tubular arrays was analyzed by elemental mappings of the electron energy loss spectroscope. As depicted in Figure 3b, it appears that elements of Zn, Mn, and O are distributed uniformly across the tubular walls. Because the initial ZnO template was gradually transformed to the $ZnMn_2O_4$ tubular array structure with an increased reaction time, there could be a difference between the diffusion rates of Zn^{2+} and Mn^{2+} in an aqueous solution.[34−37] In this regard, a tentative formation scheme for the $ZnMn_2O_4$ tubular arrays is illustrated in Scheme 1, based on the SEM, XRD, Raman, and TEM measurements. Scheme 1a represents the ZnO nanorod templates grown on the Ti substrate by the hydrothermal process.[29] In $Mn(CH_3COO)_2$ aqueous solution, the different cation exchange rates between the faster outward transport (Zn^{2+}) and the relatively slower inward diffusion (Mn^{2+}) could drive a discrepancy on the net mass transport between the internal and external parts of the ZnO nanorod and the Zn-Mn-O hollow structure, as shown in Scheme 1b, which could give rise to void or vacancy formation inside the nanorod structure.[34,35,45] During the cation exchange reactions, the chemical potential difference between the inner and outer phases leads to cation diffusion effects, and this diffusion process takes place until the reaction is complete.[34−36] Eventually, the hollow parts of the $ZnMn_2O_4$ arrays were formed with

Scheme 1. (a−c) Illustration of the Possible Formation Scheme of $ZnMn_2O_4$ Tubular Arrays from ZnO Nanorod Arrays. (d) Illustration of Hypothetical Charging Process over the $ZnMn_2O_4$ Mesoscale Tubular Arrays during Cycling

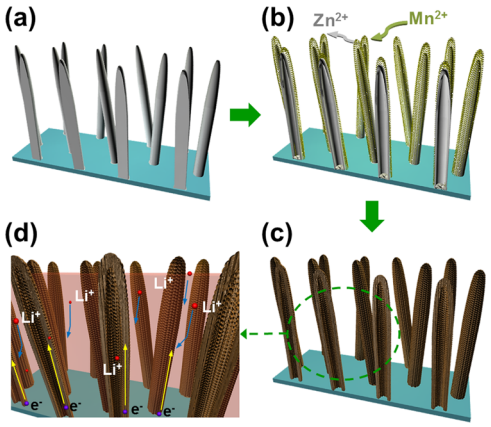

continuous reaction, as demonstrated in the TEM analysis shown in Figure 1c.

To further examine the oxidation state and atomic ratio of Zn and Mn elements in the as-prepared $ZnMn_2O_4$ mesoscale tubules, XPS analysis was conducted, as shown in Figure 4a, which exhibits photoelectron spectra for elements of Zn, Mn, and O. In Figure 4b, the peaks of 653.5 and 641.6 eV can be attributed to Mn $2p_{1/2}$ and Mn $2p_{3/2}$, respectively. The binding energy separation between these two peaks is 11.9 eV, which is consistent with that of $ZnMn_2O_4$ materials.[16−25] Figure 4c depicts Zn 2p spectra at binding energies of 1044.3 and 1021.2 eV, which can be ascribed to Zn $2p_{1/2}$ and Zn $2p_{3/2}$, respectively. Additionally, the energy difference between the Zn $2p_{1/2}$ and Zn $2p_{3/2}$ peaks is 23.1 eV, which is in line with previous reports[42,44] and reveals that the oxidation state of Mn is +3 in the $ZnMn_2O_4$ phase. As shown in Figure 4d, the O 1s peak is deconvoluted into two peaks: one peak at 530.8 eV corresponds to the lattice oxygen in $ZnMn_2O_4$, while the other peak at 529.8 eV is attributed to oxygen in carbonate species on the $ZnMn_2O_4$ surface.[42,44] From the peak areas of the XPS spectra, the surface composition of Zn:Mn:O elements appeared to be 1:1.61:3.81, which is close to the stoichiometry of the $ZnMn_2O_4$ phase.

The electrochemical properties of the as-prepared $ZnMn_2O_4$ array electrodes were investigated using CVs and galvanostatic charge/discharge measurements. Figure 5a shows the CVs for $ZnMn_2O_4$ array electrodes measured at a scan rate of 0.05 mV s^{-1} in the potential range of 3.0−0.01 V (versus Li/Li^+) whose CV profiles are similar to those previously reported for the $ZnMn_2O_4$ electrode systems.[16−25] The following equations represent consecutive conversion reactions by Li^+ with $ZnMn_2O_4$ materials that are involved in the CV profiles.[16−18]

The first discharge:

$$ZnMn_2O_4 + 9Li^+ + 9e^- \rightarrow ZnLi + 2Mn + 4Li_2O \quad (1)$$

Reversible reactions:

$$ZnO + 2Li^+ + 2e^- \rightleftarrows Zn + Li_2O \quad (2)$$

$$2MnO + 4Li^+ + 4e^- \rightleftarrows 2Mn + 2Li_2O \quad (3)$$

$$Zn + Li^+ + e^- \rightleftarrows ZnLi \quad (4)$$

The first CV profile is considerably different from subsequent cycles, which indicates that a different Li^+ storage mechanism is

dx.doi.org/10.1021/am403546s | ACS Appl. Mater. Interfaces 2013, 5, 11321−11328

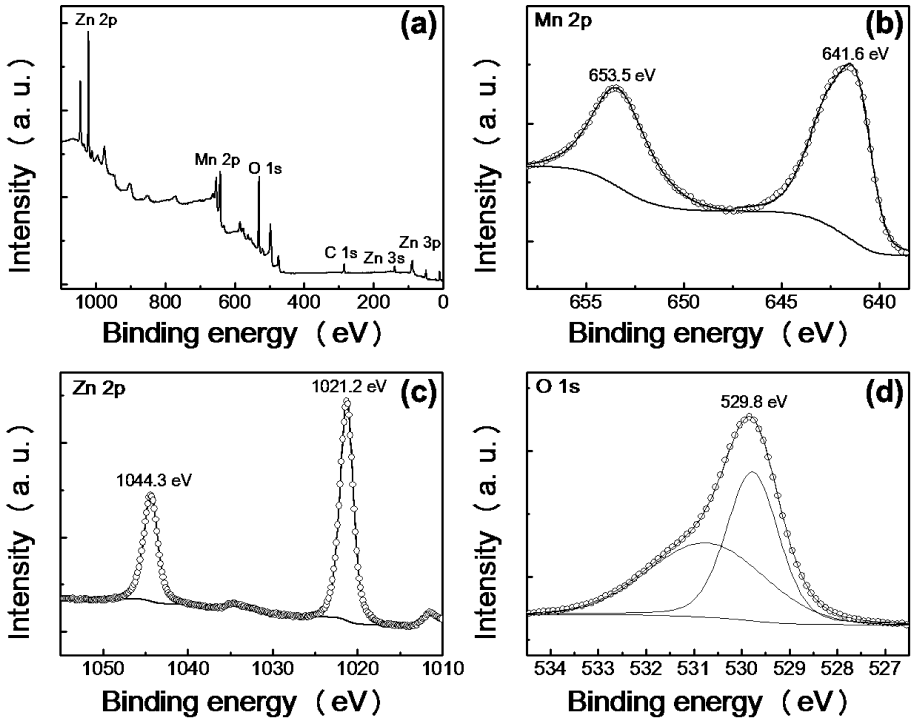

Figure 4. XPS spectra of (a) full scan, (b) Mn 2p, (c) Zn 2p, and (d) O 1s regions of the $ZnMn_2O_4$ mesoscale tubular arrays.

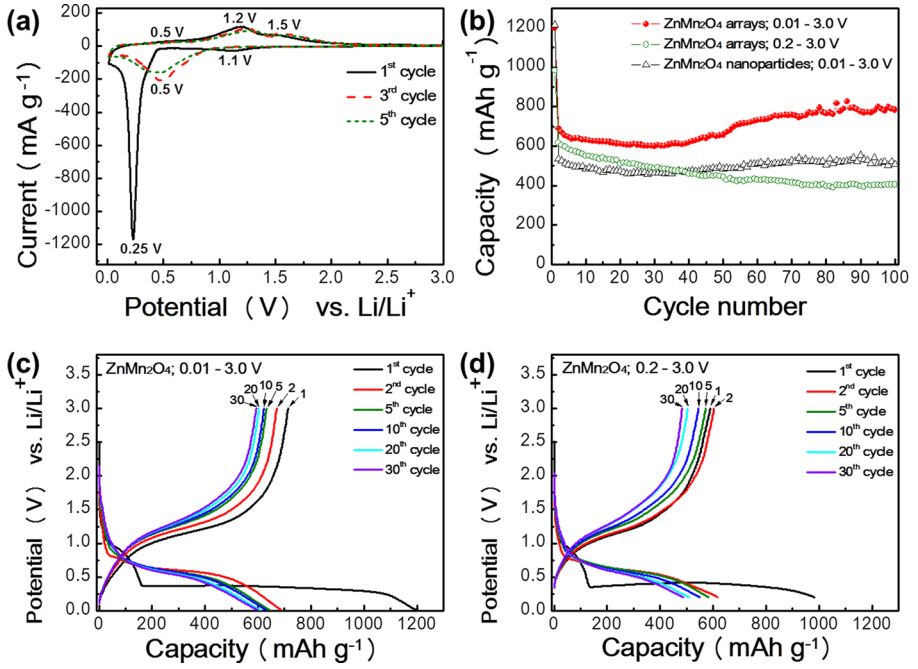

Figure 5. (a) CVs of $ZnMn_2O_4$ tubular array electrodes between 3.0 and 0.01 V at a scan rate of 0.05 mV s^{-1}. (b) Discharge capacity−cycle number curves of $ZnMn_2O_4$ tubular arrays and $ZnMn_2O_4$ nanoparticles in the potential window of 0.01−3.0 or 0.2−3.0 V. Voltage profiles of the $ZnMn_2O_4$ tubular array electrode at a current rate of 100 mA g^{-1} in the potential windows of (c) 0.01−3.0 V and (d) 0.2−3.0 V.

involved in the first cycle compared with the subsequent cycles. In the first cathodic sweep, the CVs show a broad peak at approximately 1.1 V, which is ascribed to the reduction of Mn^{3+} to Mn^{2+} and to the irreversible decomposition of the electrolyte solvent to form the solid electrolyte interphase (SEI) layers. Another strong cathodic peak at 0.25 V corresponds to the reduction processes of Mn^{2+} and Zn^{2+} to metallic Mn^0 and Zn^0. Moreover, relatively weak and broad peaks were observed below 0.25 V, which are related to the formation of a ZnLi alloy, like eq 1.[16−18] In the first anodic sweep, the wide oxidation peak at approximately 0.5 V corresponds to the Li^+ dealloying from the ZnLi alloy formed in the reductive sweep, according to eq 4.[22] The peaks at approximately 1.2 V can be attributed to the oxidation of metallic Mn^0 to Mn^{2+}, as indicated in eq 3, and the peaks at approximately 1.5 V can be attributed to the oxidation of metallic Zn^0 to Zn^{2+} along with the decomposition of the Li_2O matrix, according to eq 2.[23] In subsequent cycles, the cathodic peak shifts from 0.25 to 0.5 V,

which could be associated with structural rearrangement.[16−18] Conversely, the following anodic peaks are similar to those obtained in the first scan, suggesting identical electrochemical reactions for the anodic scans.[23−25] Remarkably, there is no noticeable change in the oxidation and reduction currents after the first cycle, indicating high reversibility and structural durability of the electrode reactions after the first cycle.[29,30] Additionally, the difference between the CV profiles of the $ZnMn_2O_4$ tubule and ZnO nanorod electrodes (see Figure S3 in the Supporting Information) could allow one to infer that the ZnO nanorods are totally converted to $ZnMn_2O_4$ tubules. Figure 5b shows the galvanostatic cycling curves for the $ZnMn_2O_4$ mesoscale tubular array electrodes up to 100 cycles at a current density of 100 mA g^{-1} at room temperature in a voltage range from 0.01 to 3.0 V (versus Li/Li^+). The initial discharge capacity of the $ZnMn_2O_4$ tubular array electrode was 1198.3 mAh g^{-1}, and a high discharge capacity of 784.3 mAh g^{-1} was retained even after 100 cycles. This reversible capacity value is much higher than that of commercial graphite electrodes (372 mAh g^{-1}). For comparison, we also tested the $ZnMn_2O_4$ nanoparticles and ZnO nanorod arrays (see Figure S4 in the Supporting Information) under identical test conditions. The $ZnMn_2O_4$ nanoparticles showed a low discharge capacity compared to the $ZnMn_2O_4$ mesoscale tubular arrays; the discharge capacity of $ZnMn_2O_4$ nanoparticles after 100 cycles was 507.5 mAh g^{-1}, indicating that the hollow array structure proposed here would be much more suitable to store Li^+ with high cyclic durability during repeated charge/discharge cycles. Interestingly, the discharge capacity of the $ZnMn_2O_4$ tubular array electrode appears to increase gradually after 40 cycles. It has been reported that transition-metal oxides, such as CoO,[46] Co_3O_4,[47] Mn_3O_4,[9] and Fe_3O_4,[43,48] often appear to show a gradual capacity increase during repeated charge/discharge cycling. It is known that this phenomenon is related to the reversible formation and dissolution of a polymeric gel-like film, resulting from the electrolyte reduction by Li metal, which could also reversibly store Li^+.[49−51] The polymeric gel-type layer on the metal nanoparticles could be formed due to the reduction of the electrolyte at potentials lower than 0.7 V (versus Li/Li^+), while this layer could be reversibly dissolved at oxidation potentials higher than 2.0 V.[52−54] To elucidate the gradual capacity increase and the significant improvement of cycling stability observed for $ZnMn_2O_4$ mesoscale tubular array electrodes, we further tested the galvanostatic charge/discharge of these electrodes in a voltage range of 0.2−3.0 V at a constant current density of 100 mA g^{-1}. We selected this lower cut-off potential of 0.2 V because the polymeric gel-type layer could be formed at the potential below 0.25 V, as shown in the CV profiles of Figure 5a. In Figure 5b, the reversible discharge capacity was decreased continuously (see the empty circles), in contrast to the case of deep charge/discharge conditions with the cut-off potentials of 0.01−3.0 V. It can be concluded that the polymeric gel-type layer on the electrode surface could enhance the mechanical cohesion between the nanograins in the electrode and that this layer is thus helpful in maintaining good cycling durability.[52−54] Note that the $ZnMn_2O_4$ tubular array electrode shows a considerably higher initial Coulombic efficiency (59.5 %) than the $ZnMn_2O_4$ nanoparticle electrode (42.0 %). Thereafter, the Coulombic efficiency of the $ZnMn_2O_4$ tubular array electrode increases to 97.2 % in the second cycle and then holds at a steady value (see Figure S5 in the Supporting Information), indicating a high reversibility of the electrode reaction after the first cycle, which is also consistent with CV profiles. Figure 5c shows the voltage−capacity profiles of the $ZnMn_2O_4$ tubular array electrodes at a rate of 100 mA g^{-1} in the potential range of 0.01−3.0 V. During the first discharge, the voltage profile shows a small plateau around 1.0 V arising from the reduction of Mn^{3+} to Mn^{2+} and SEI layer formation. Another pronounced plateau at approximately 0.3 V is related to the formations of metallic Mn^0 and Zn^0 dispersed in the matrix of Li_2O, which is consistent with the earlier CV profiles. The voltage−capacity profiles of the $ZnMn_2O_4$ tubular array electrode between 0.2 and 3.0 V in Figure 5d are qualitatively similar to those in Figure 5c; however, the charge/discharge capacity at the cut-off potentials of 0.2−3.0 V was found to decrease continuously.

In addition to the high specific capacity and cycling stability, the high rate performance of the electrode is also of great importance, especially for high-power devices. Therefore, we further investigated the rate capability of the $ZnMn_2O_4$ electrode at various current densities, as shown in Figure 6.

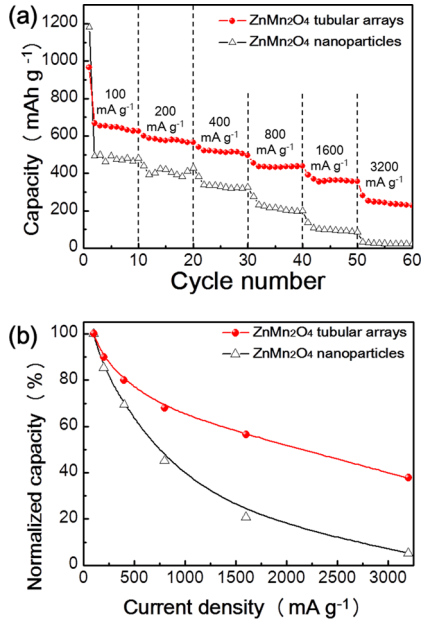

Figure 6. (a) Cycling performance of $ZnMn_2O_4$ tubular arrays together with $ZnMn_2O_4$ nanoparticles at various current rates (100, 200, 400, 800, 1600, and 3200 mA g^{-1}) between 0.01 and 3.0 V. (b) Normalized capacity at each step by the average capacity values under a 100 mA g^{-1} current density of the first step.

Two samples of the $ZnMn_2O_4$ tubular array and nanoparticle electrode were cycled from a current density of 100 with a stepwise increment of 100 up to 3200 mA g^{-1}. For the current densities of 100, 200, 400, 800, 1600, and 3200 mA g^{-1}, the $ZnMn_2O_4$ tubular array electrode was able to deliver average discharge capacities of 644.6, 578.8, 515.9, 437.5, 363.6, and 243.5 mAh g^{-1}, respectively, whereas the $ZnMn_2O_4$ nanoparticle electrode delivered decreased average discharge capacities of 480.3, 410.3, 333.8, 216.8, 100.0, and 25.5 mAh g^{-1}, respectively. It is noted that the normalized capacity of the $ZnMn_2O_4$ tubular array electrode (37.8 %) is much higher than that of the $ZnMn_2O_4$ nanoparticle electrode (5.3 %) at a high current density of 3200 mA g^{-1}, as shown in Figure 6b. Therefore, as the charge/discharge rate increased, the capacity fade of the $ZnMn_2O_4$ tubular array electrode was significantly reduced compared to that of the $ZnMn_2O_4$ nanoparticle electrode. These remarkable improvements suggest that the $ZnMn_2O_4$ tubular array structure may not be destroyed, even at such a high

current density of 3200 mA g^{-1} (or 14.7 min per half-cycle) (see Figure S6 in the Supporting Information), thus indicating good electrochemical reversibility and structural durability. The enhanced rate capability of the $ZnMn_2O_4$ tubular electrodes could be attributed to their unique hollow architectures. Specifically, the open space between individual 1D $ZnMn_2O_4$ arrays can provide better electrolyte permeability and a shorter Li^+ diffusion path.[29,30] Therefore, the structure of $ZnMn_2O_4$ arrays could mitigate mechanical stress effectively during repeated charge/discharge processes, which eventually contributes to the cyclic durability. The major drawback of transition-metal oxide-based electrodes is their poor kinetics for Li^+ transport compared to the intercalation electrodes for use in LIBs.[55] As shown in Figure S7 (Supporting Information), the voltage hysteresis decreased from 0.93 V for the $ZnMn_2O_4$ nanoparticles to 0.85 V for the $ZnMn_2O_4$ tubular arrays based on the first charge/discharge profiles at a current density of 100 mA g^{-1}. This result is an indication of the advanced Li^+ storage reaction kinetics in the $ZnMn_2O_4$ mesoscale tubular array electrodes.

Consequently, as depicted in Scheme 1d, the high lithium storage performance of the $ZnMn_2O_4$ tubular array electrodes could be ascribed to their unique architecture as follows: (i) hollow channels along the 1D array structure can effectively accommodate the mechanical stress during repeated charge/discharge processes; (ii) the free-standing array architecture may enable most of the $ZnMn_2O_4$ mesoscale tubules to participate in the electrochemical reactions because the entire $ZnMn_2O_4$ tubular arrays are in electrical contact with the Ti current collector; (iii) open interspace between the $ZnMn_2O_4$ tubular arrays can enhance the wetting properties of electrolytes and accommodate mechanical stress during charge/discharge processes; and (iv) the large electrode/electrolyte contact area originating from both the hollow natures and array structure can provide a short pathway for Li^+ diffusion, thus improving the lithium storage capacity, rate capability, and cycling durability.[56,57]

CONCLUSIONS

In conclusion, we have reported on $ZnMn_2O_4$ mesoscale tubular arrays grown on Ti substrates and used directly as an anode for LIBs without any ancillary materials of conductive carbon and cohesive binder. The $ZnMn_2O_4$ tubular array electrode showed a high initial discharge capacity (1198.3 mAh g^{-1}), excellent capacity retention, and high rate capability. The enhanced lithium storage properties of $ZnMn_2O_4$ mesoscale tubular array electrodes are related to their unique structural features, such as the presence of hollow space in the tubule structure with proper intervals between the tubular arrays, facilitated Li^+ diffusion, as well as alleviation of the mechanical stress caused by repeated charge/discharge processes. Thus, the $ZnMn_2O_4$ mesoscale tubular arrays, with high energy and power density, could be a promising potential anode system for next-generation LIBs that can outperform current materials.

ASSOCIATED CONTENT

Supporting Information

TEM images and additional electrochemical data. This material is available free of charge via the Internet at http://pubs.acs.org.

AUTHOR INFORMATION

Corresponding Author

*Tel: +82-62-715-2317. Fax: +82-62-715-2304. E-mail: wbkim@gist.ac.kr.

Notes

The authors declare no competing financial interest.

ACKNOWLEDGMENTS

This work was supported by the National Research Foundation of Korea (NRF) grant funded by the Korea government (MSIP) (No. 2013029776 (Mid-career Researcher Program)) and by the Global Frontier R&D Program (0420-20120126) on Center for Multiscale Energy System through NRF. We also appreciate the financial support by the Core Technology Development Program from the Research Institute for Solar and Sustainable Energies (RISE/GIST).

REFERENCES

(1) Poizot, P.; Laruelle, S.; Grugeon, S.; Dupont, L.; Tarascon, J.-M. *Nature* **2000**, *407*, 496−499.
(2) Mai, Y. J.; Wang, X. L.; Xiang, J. Y.; Qiao, Y. Q.; Zhang, D.; Gu, C. D.; Tu, J. P. *Electrochim. Acta* **2011**, *56*, 2306−2311.
(3) Zheng, S.-F.; Hu, J.-S.; Zhong, L.-S.; Song, W.-G.; Wan, L.-J.; Guo, Y.-G.; Guo, Y.-G. *Chem. Mater.* **2008**, *20*, 3617−3622.
(4) Shi, W.; Zhu, J.; Sim, D. H.; Tay, Y. Y.; Lu, Z.; Zhang, X.; Sharma, Y.; Srinivasan, M.; Zhang, H.; Hng, H. H.; Yan, Q. *J. Mater. Chem.* **2011**, *21*, 3422−3427.
(5) Ma, Y.; Zhang, C.; Ji, G.; Lee, J. Y. *J. Mater. Chem.* **2012**, *22*, 7845−7850.
(6) Nam, S. H.; Kim, Y. S.; Shim, H.-S.; Kim, J. G.; Kim, W. B. *Nanoscale Res. Lett.* **2011**, *6*, 292.
(7) Wang, X.; Li, X.; Sun, X.; Li, F.; Liu, Q.; Wang, Q.; He, D. *J. Mater. Chem.* **2011**, *21*, 3571−3573.
(8) Huang, X. H.; Xia, X. H.; Yuan, Y. F.; Zhou, F. *Electrochim. Acta* **2011**, *56*, 4960−4965.
(9) Wang, H.; Cui, L.-F.; Yang, Y.; Casalongue, H. S.; Robinson, J. T.; Liang, Y.; Cui, Y.; Dai, H. *J. Am. Chem. Soc.* **2010**, *132*, 13978−13980.
(10) Li, L.; Guo, Z.; Du, A.; Liu, H. *J. Mater. Chem.* **2012**, *22*, 3600−3605.
(11) Gao, J.; Lowe, M. A.; Abruña, H. D. *Chem. Mater.* **2011**, *23*, 3223−3227.
(12) Kim, J. G.; Nam, S. H.; Lee, S. H.; Choi, S. M.; Kim, W. B. *ACS Appl. Mater. Interfaces* **2011**, *3*, 828−835.
(13) Nam, S. H.; Kim, K. S.; Shim, H.-S.; Lee, S. H.; Jung, G. Y.; Kim, W. B. *Nano Lett.* **2011**, *11*, 3656−3662.
(14) Zhou, L.; Zhao, D.; Lou, X. W. *Adv. Mater.* **2012**, *24*, 745−748.
(15) Courtel, F. M.; Duncan, H.; Abu-Lebdeh, Y.; Davidson, I. J. *J. Mater. Chem.* **2011**, *21*, 10206−10218.
(16) Deng, Y.; Tang, S.; Zhang, Q.; Shi, Z.; Zhang, L.; Zhan, S.; Chen, G. *J. Mater. Chem.* **2011**, *21*, 11987−11995.
(17) Kim, S.-W.; Lee, H.-W.; Muralidharan, P.; Seo, D.-H.; Yoon, W.-S.; Kim, D. K.; Kang, K. *Nano Res.* **2011**, *4*, 505−510.
(18) Xiao, L.; Yang, Y.; Yin, J.; Li, Q.; Zhang, L. *J. Power Sources* **2009**, *194*, 1089−1093.
(19) Ma, Y.; Ji, G.; Lee, J. Y. *J. Mater. Chem.* **2011**, *21*, 13009−13014.
(20) Yang, Y.; Zhao, Y.; Xiao, L.; Zhang, L. *Electrochem. Commun.* **2008**, *10*, 1117−1120.
(21) Zhang, G.; Yu, L.; Wu, H. B.; Hoster, H. E.; Lou, X. W. *Adv. Mater.* **2012**, *24*, 4609−4613.
(22) Zhou, L.; Wu, H. B.; Zhu, T.; Lou, X. W. *J. Mater. Chem.* **2012**, *22*, 827−829.
(23) Courtel, F. M.; Abu-Lebdeh, Y.; Davidson, I. J. *Electrochim. Acta* **2012**, *71*, 123−127.
(24) Zhao, J.; Wang, F.; Su, P.; Li, M.; Chen, J.; Yang, Q.; Li, C. *J. Mater. Chem.* **2012**, *22*, 13328−13333.
(25) Bai, Z.; Fan, N.; Sun, C.; Ju, Z.; Guo, C.; Yang, J.; Qian, Y. *Nanoscale* **2013**, *5*, 2442−2447.
(26) Cheng, F.; Tao, Z.; Liang, J.; Chen, J. *Chem. Mater.* **2008**, *20*, 667−681.

(27) Lee, B.-S.; Son, S.-B.; Park, K.-M.; Yu, W.-R.; Oh, K.-H.; Lee, S.-H. *J. Power Sources* **2012**, *199*, 53−60.
(28) Lee, B.-S.; Son, S.-B.; Seo, J.-H.; Park, K.-M.; Lee, G.; Lee, S.-H.; Oh, K. H.; Ahn, J.-P.; Yu, W.-R. *Nanoscale* **2013**, *5*, 4790−4796.
(29) Kim, J. G.; Lee, S. H.; Nam, S. H.; Choi, S. M.; Kim, W. B. *RSC Adv.* **2012**, *2*, 7829−7836.
(30) Liu, J.; Li, Y.; Fan, H.; Zhu, Z.; Jiang, J.; Ding, R.; Hu, Y.; Huang, X. *Chem. Mater.* **2010**, *22*, 212−217.
(31) Wang, Z.; Zhou, L.; Lou, X. W. *Adv. Mater.* **2012**, *24*, 1903−1911.
(32) Huang, T.; Qi, L. *Nanotechnology* **2009**, *20*, 025606.
(33) Tian, L.; Yang, X.; Lu, P.; Williams, I. D.; Wang, C.; Ou, S.; Liang, C.; Wu, M. *Inorg. Chem.* **2008**, *47*, 5522−5524.
(34) Kim, J. W.; Shim, H.-S.; Ko, S. W.; Jeong, U.; Lee, C.-L.; Kim, W. B. *J. Mater. Chem.* **2012**, *22*, 20889−20895.
(35) Shim, H.-S.; Shinde, V. R.; Kim, J. W.; Gujar, T. P.; Joo, O.-S.; Kim, H. J.; Kim, W. B. *Chem. Mater.* **2009**, *21*, 1875−1883.
(36) Zhang, F.; Shi, Y.; Sun, X.; Zhao, D.; Stucky, G. D. *Chem. Mater.* **2009**, *21*, 5237−5243.
(37) Rivest, J. B.; Jain, P. K. *Chem. Soc. Rev.* **2013**, *42*, 89−96.
(38) Fan, H. J.; Knez, M.; Scholz, R.; Nielsch, K.; Pippel, E.; Hesse, D.; Zacharias, M.; Gösele, U. *Nat. Mater.* **2006**, *5*, 627−631.
(39) Chow, L.; Lupan, O.; Heinrich, H.; Chai, G. *Appl. Phys. Lett.* **2009**, *94*, 163105.
(40) Rubio-Marcos, F.; Quesada, A.; García, M. A.; Bañares, M. A.; Fierro, J. L. G.; Martín-Gonzalez, M. S.; Costa-Krämer, J. L.; Fernández, J. F. *J. Solid State Chem.* **2009**, *182*, 1211−1216.
(41) Malavasi, L.; Galinetto, P.; Mozzati, M. C.; Azzoni, C. B.; Flor, G. *Phys. Chem. Chem. Phys.* **2002**, *4*, 3876−3880.
(42) Li, H.; Song, B.; Wang, W. J.; Chen, X. L. *Mater. Chem. Phys.* **2011**, *130*, 39−44.
(43) Samanta, K.; Dussan, S.; Bhattacharya, P.; Katiyar, R. S. *Appl. Phys. Lett.* **2007**, *90*, 261903.
(44) Zhang, P.; Li, X.; Zhao, Q.; Liu, S. *Nanoscale Res. Lett.* **2011**, *6*, 323.
(45) Duan, C. J.; Delsing, A. C. A.; Hintzen, H. T. *Chem. Mater.* **2009**, *21*, 1010−1016.
(46) Do, J.-S.; Weng, C.-H. *J. Power Sources* **2005**, *146*, 482−486.
(47) Shaju, K. M.; Jiao, F.; Débart, A.; Bruce, P. G. *Phys. Chem. Chem. Phys.* **2007**, *9*, 1837−1842.
(48) Zhou, G.; Wang, D.-W.; Li, F.; Zhang, L.; Li, N.; Wu, Z.-S.; Wen, L.; Lu, G. Q.; Cheng, H.-M. *Chem. Mater.* **2010**, *22*, 5306−5313.
(49) Wang, Y.; Su, D.; Ung, A.; Ahn, J.-H.; Wang, G. *Nanotechnology* **2012**, *23*, 055402.
(50) Sharma, N.; Shaju, K. M.; Rao, G. V. S.; Chowdari, B. V. R. *Electrochim. Acta* **2004**, *49*, 1035−1043.
(51) Cabana, J.; Monconduit, L.; Larcher, D.; Palacín, M. R. *Adv. Mater.* **2010**, *22*, E170−E192.
(52) Sharma, Y.; Sharma, N.; Rao, G. V. S.; Chowdari, B. V. R. *Adv. Funct. Mater.* **2007**, *17*, 2855−2861.
(53) Laruelle, S.; Grugeon, S.; Poizot, P.; Dolle, M.; Dupont, L.; Tarascon, J.-M. *J. Electrochem. Soc.* **2002**, *149*, A627−A634.
(54) Lu, Y.; Wang, X.; Mai, Y.; Xiang, J.; Zhang, H.; Li, L.; Gu, C.; Tu, J.; Mao, S. X. *J. Phys. Chem. C* **2012**, *116*, 22217−22225.
(55) Chae, C.; Kim, J. H.; Kim, J. M.; Sun, Y.-K.; Lee, J. K. *J. Mater. Chem.* **2012**, *22*, 17870−17877.
(56) Li, Y.; Tan, B.; Wu, Y. *Nano Lett.* **2008**, *8*, 265−270.
(57) Liu, J.; Li, Y.; Huang, X.; Ding, R.; Hu, Y.; Jiang, J.; Liao, L. *J. Mater. Chem.* **2009**, *19*, 1859−1864.